Wave Motion 67 (2016) 121–140

Contents lists available at ScienceDirect

Wave Motion

journal homepage: www.elsevier.com/locate/wavemoti

A comparison of time-reversal and inverse-source methods for the optimal delivery of wave energy to subsurface targets

Seungbum Koo [a], Pranav M. Karve [a], Loukas F. Kallivokas [a,b,*]

[a] Department of Civil, Architectural and Environmental Engineering, The University of Texas at Austin, 301 East Dean Keeton St., Stop C1747, Austin, TX 78712, USA

[b] The Institute for Computational Engineering and Sciences (ICES), The University of Texas at Austin, 201 East 24th St., Stop C0200, Austin, TX 78712, USA

HIGHLIGHTS

- Wave energy focusing to targets in heterogeneous, semi-infinite, elastic media.
- Comparison of time-reversal and inverse-source methods for optimal source design.
- Time-reversal and inverse-source yield similar energy delivery efficiency.

ARTICLE INFO

Article history:
Received 10 May 2016
Received in revised form 24 July 2016
Accepted 26 July 2016
Available online 5 August 2016

Keywords:
Wave energy focusing
Time reversal
Inverse-source modeling
Subsurface targets
Optimal source design

ABSTRACT

Elastic wave stimulation of targets embedded in heterogeneous elastic solids has potential applications in medicine (treatment of tumors, lithotripsy), petroleum engineering, environmental engineering, hydro-geology, etc. Systematic methodologies for designing the wave sources that focus optimally the emitted energy into the target zone are important for ensuring the efficiency of the wave energy delivery process. In this article, we compare two methodologies that could be used for designing wave sources that maximize wave-based stimulation of the target region: a time-reversal (TR) approach and an inverse-source (IS) approach. The former relies on the linearity and reciprocity admitted by the governing physics, and the latter is an optimization-based framework that attempts maximization of a wave motion metric in the target zone. Whereas closed cavity problems are easier to treat, here we concentrate on the challenging problem of wave energy focusing to subsurface geo-formations using motion actuators placed on the ground surface. We formulate the underlying wave propagation problem for two-dimensional, semi-infinite, elastic, heterogeneous domains. We define motion metrics to measure the energy expended by the wave sources, and the kinetic energy delivered to the target formation. We conduct numerical experiments and compare the relative performance of the wave sources designed using the TR and the IS approaches. Both methods have advantages and disadvantages: for remote targets in well-characterized formations IS is preferred; whereas TR is preferable when a source can be embedded in the target. Both methods have similar efficiency.

* Corresponding author at: Department of Civil, Architectural and Environmental Engineering, The University of Texas at Austin, 301 East Dean Keeton St., Stop C1747, Austin, TX 78712, USA.
E-mail addresses: seungbum.koo@utexas.edu (S. Koo), pranav.karve@utexas.edu (P.M. Karve), loukas@mail.utexas.edu (L.F. Kallivokas).

http://dx.doi.org/10.1016/j.wavemoti.2016.07.011
0165-2125/

1. Introduction

Stress wave stimulation of a *target zone* in a heterogeneous solid can be a potent, non-invasive recourse for bringing about desired changes in the mechanical behavior of the target. Some key applications of wave stimulation include wave-based enhanced oil recovery (EOR), treatment of tumors and lithotripsy, forced detonation of unexploded ordnances, removal of contaminants from aquifers, and others. Broadly speaking, the success of the aforementioned applications hinges on two types of phenomena: (a) the local behavior, which dictates the intensity of the stimulation required to effect the desired change, and (b) the global behavior, which is concerned with the ability of the wave sources to deliver stimulation of a required magnitude in the presence of application-specific constraints (wave source amplitudes, wave source locations, attenuation, etc.). In general, the local phenomena are governed by microscopic material behavior (pore-scale effects in geophysics, cellular behavior in medical applications, etc.), whereas the global phenomena depend on the macroscopic aspects (the wave path, heterogeneity, constructive/destructive interference, etc.) of wave propagation. This article is concerned with the second aspect (global, or macroscopic) of wave energy delivery. Specifically, we discuss and compare two candidate methodologies, a time-reversal-based approach and an inverse-source approach that can be used for designing wave sources that focus energy to the target zone. In the following, we review the salient features of both methodologies.

The time-reversal method (TR) [1–6] can be used to direct the wave energy towards scatterers or inclusions embedded in an acoustic or an elastic medium. Typical applications of TR include source localization [7,8], crack and defect identification [9,10], land-mine detection [11], wave energy focusing [12], etc. The TR method for focusing wave energy to a target zone consists of two steps. In a first step, the boundary of the (acoustic or elastic) domain of interest, or a part of it, is populated with a receiver array (the time-reversal mirror [2,13]), and a source is placed in the target. The waves emitted by the source are recorded by the receiver array. In a second step, the signals recorded at the receivers are time-reversed, and broadcast back from their respective locations. The signals recorded on the boundary of the medium contain the information about the path the waves traversed. When the mirror-recordings are time-reversed, the emitted waves home in to the location of the original source, i.e., the waves *refocus*. The intensity of the refocus can be ascertained by measuring/computing a motion metric at the target zone. We note that the heterogeneity of the medium does not hinder, but rather enhances the quality of the refocus due to the elongation of the wave path caused by steering and reflection [14]. If one records the waves arriving at the mirror for a sufficiently long time, then waves radiating from the mirror are reflected back to the mirror due to the medium's heterogeneity. Consequently, the record at the mirror has more information compared to what it would have had for a homogeneous medium, and, typically, the quality of the refocus is enhanced [14,15]. Thus, the TR method is a self-adaptive method that accounts for the heterogeneity of the medium [2,13,16]. We remark that an ideal implementation of the TR method requires a perfect mirror, which means that the mirror must cover the entire boundary of the medium. In practice, however, a limited number of sensors, situated only on part of the boundary would be sufficient. Even with this limitation, time-reversal methods work well for focusing if a sufficient time is allowed for the waves to reflect, to change direction, and to reach the boundary where the sensors are placed [3,15,17]. Note that placing wave sources in the target zone may be infeasible or impractical for some applications. In this case, the first TR step can be performed in a numerical simulation.[1] The computed displacement time histories at sensor locations can be time-reversed, and used as source excitations to achieve the desired focusing. Thus, the computational cost of the TR method is (approximately) that of a forward problem solution. Furthermore, if the application at hand allows placement of a wave source in the target zone, then the TR method does not require any *a priori* knowledge of the material and geometric properties of the domain of interest.

Alternatively, wave sources that focus the wave energy to a target subsurface formation can be designed by solving an inverse-source (IS) problem. In previous work in our group [18–21], we formulated an inverse-source problem for wave energy focusing as a constrained minimization problem, where minimization of a suitably defined objective functional is tantamount to the maximization of the wave motion within the target zone, and the equations of the governing physics are side-imposed as constraints. This approach assumes that the material and geometric properties of the domain of interest are known, and aims at finding the optimal source time signals and source locations that maximize the predefined motion metric of the target. The inversion methodology for computing the optimal source parameters faces two key challenges: (a) the solution of the constrained minimization problem is computationally demanding for large elastodynamic systems, and (b) the method assumes *a priori* knowledge of the heterogeneous domain of interest, which is difficult to obtain in practice. However, uncertainties in the material distribution can be addressed, and an assessment of the effect of the uncertainty on the energy delivery efficiency is possible [22].

Thus, both the TR and the IS methodologies can potentially be used to design wave sources that focus wave energy to a targeted subsurface formation. It is unclear though whether the sources designed using the computationally inexpensive TR method will be able to deliver sufficient amount of wave energy to the target zone in a semi-infinite, elastic medium. On the other hand, the optimization-based inversion approach is computationally demanding for large elastodynamic systems. Hence, it is of interest to investigate the relative effectiveness of the two methodologies for geophysical applications. With the notable exception of Levi et al. [23], who reported on TR-based scatterer location recovery in semi-infinite elastic media, the TR method has not been studied for semi-infinite, elastic solids. The key challenges for using time-reversal in semi-infinite, elastic domains include:

[1] Only when the material/geometric description of the domain is known *a priori* with sufficient resolution.

- In semi-infinite media, the only viable location for placing the time-reversal mirror is the free (ground) surface. Thus, most of the wave energy emitted by the source in the first step of TR will not reach the TR mirror. This, in turn, affects the refocusing adversely.
- In the first step of TR, the displacement time histories are recorded by the sensors installed on the free surface of the semi-infinite domain of interest. An ideal implementation of the TR method requires enforcement of the time-reversed version of the recorded displacement as a Dirichlet boundary condition on the free surface. However, implementing a Dirichlet boundary condition on the free surface of a heterogeneous, elastic half space is impossible in practice: one can only apply forces (tractions) during the time-reversal step. Therefore, here, we apply the time-reversed Dirichlet boundary condition as a Neumann boundary condition. This application-driven modification in the field implementation of the TR method worsens the refocusing quality [13].

In this article, we show that despite the aforementioned challenges, the wave sources designed using the TR method are able to focus the wave energy to the target region in a semi-infinite, elastic solid. In the TR literature, the pressure or displacement amplitude at the target location is compared to the corresponding amplitudes in the rest of the domain to ascertain the presence of refocusing and to assess the refocusing quality. A higher amplitude at the target is (rightfully) considered as an evidence of refocusing. Thus, typically, the success of the TR methodology is ascertained using a *relative* metric of the wave motion in the domain. For the success of applications of wave energy focusing in semi-infinite media, the wave motion amplitude in the target has to exceed the threshold dictated by the local, or the micro-scale, behavior. That is, the success of the applications depends mainly on the *absolute* value of the pertinent motion metric in the target, and not on the contrast between the motion metrics in the target and in the rest of the domain. As the amplitude of the wave sources is restricted by practical limitations and cannot be increased indefinitely, it is important to study the absolute value of the motion metric in the target quantitatively. In this article, we measure the wave energy delivered to the target zone using a motion metric based on kinetic energy. We use the absolute value of the motion metric (and not the motion metric value in the target relative to the rest of the domain) to compare the effectiveness of wave energy delivery. We note that for the range of applications of interest that motivated this study (EOR, contaminant removal, etc.), strong stimulation of the target is paramount, and consequently, maximizing the intensity of the energy delivered at the target is a key objective.

Another key feature of the aforementioned experimental and analytical TR studies is the use of broadband (pulse-like) source excitations in the first TR step, which lead to pulse-like displacement histories at the source location after refocusing. Anderson et al. [12] studied the effect of a (monochromatic) continuous wave (CW) or a CW-like excitation on time-reversed focusing in homogeneous, finite elastic solids. They conducted laboratory experiments on a rectangular block of Berkley Blue Granite, and reported that CW-like signals can be used in the TR method to achieve spatial focusing when multiple sensors/sources are used. As far as wave energy focusing applications in geophysics (EOR, contaminant removal) are concerned, it is unclear whether a periodically applied, pulse-like excitation of the target will be sufficient to induce the desired mechanical behavior (e.g., trapped particle mobilization). A CW-like excitation may be more suitable for delivering a potent stress wave excitation to the targeted geological formation (an oil reservoir, or an aquifer). Here, we quantitatively compare the TR refocus achieved by pulse-like and CW-like excitations in heterogeneous, elastic, semi-infinite media. Thus, our main objectives are: (a) to study the quality, intensity, and efficiency of wave energy delivery achieved by wave sources designed using the TR method in semi-infinite, heterogeneous, elastic media, and (b) to compare the performance of wave sources designed using the TR and the IS methodologies.

To this end, we formulate the problem of stress wave propagation in two-dimensional, heterogeneous, isotropic, elastic, semi-infinite media. We obtain a finite computational domain by truncating the semi-infinite domain of interest using perfectly-matched-layers (PMLs) [24]. We then discuss the relevant details of the mathematical formulations and numerical implementations of the TR and IS methods [19]. Lastly, we conduct numerical experiments on a synthetically created geological formation model containing a target inclusion. In our numerical experiments, we use surface sources having a fixed maximum amplitude (50 kN/m^2) to initiate the wave motion. We define motion metrics to quantify the time-averaged kinetic energy of the target inclusion (KE_{inc}^{avg}), and the energy expended by wave sources (E_{input}). We use these metrics to study: (a) the effect of the TR mirror density in semi-infinite, layered, elastic media; (b) the potency of the stimulation delivered to the target formation by pulse-like and CW-like source excitations; and (c) the efficiency (the ratio KE_{inc}^{avg}/E_{input}) of energy delivery. We observe that: (a) the mirror density affects the intensity of refocusing, but not the quality; (b) for a fixed maximum amplitude of wave sources, the CW-like signals designed using the IS approach deliver more kinetic energy to the target; (c) the pulse-like signals obtained using the TR method are more efficient at delivering the wave energy to the target.

2. Mathematical background

In this section, we discuss the mathematical background and the details of the numerical implementation for the TR and the IS methodologies.

2.1. The time-reversal method

Here, we discuss a numerical surrogate for the experimental procedure performed in a typical laboratory/field implementation of the TR methodology. We begin our discussion by considering the ideal case of time-reversal in finite, elastic

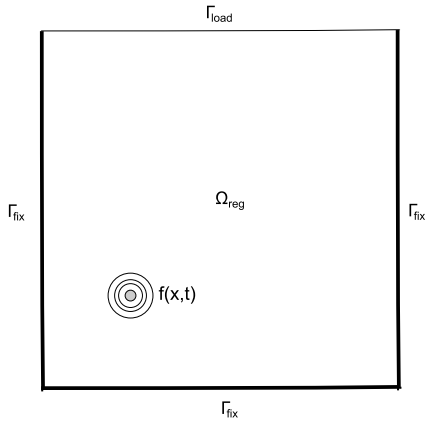

Fig. 1. A finite, homogeneous, isotropic, elastic domain.

domains. We, then, make the necessary modifications to the ideal finite-domain case in order to make it suitable for use in semi-infinite, elastic domains.

2.1.1. The time-reversal method for finite, elastic domains

Let us consider time-reversal in a finite, homogeneous, isotropic, elastic domain Ω_{reg} (Fig. 1). The equations governing the wave motion in Ω_{reg}, for time $t \in [0, T)$, are given by,

$$\mathbf{div}\,[\mu\,(\nabla\mathbf{u} + \nabla\mathbf{u}^{\intercal})] + \mathbf{div}\,[\lambda\ (\text{div}\,\mathbf{u})\ \mathbf{I}] - \rho\ddot{\mathbf{u}} + \mathbf{f} = \mathbf{0}, \quad \mathbf{x} \in \Omega_{\text{reg}}, \tag{1}$$

where, the overdot ($\dot{}$) represents the time derivative and λ and μ are Lamé parameters. As previously discussed, the TR method consists of two steps: first, a signal is initiated from within the target, and then the resulting displacement histories are recorded at the mirror (the *forward step*). Note that the spatial characteristics of the source $\mathbf{f}(\mathbf{x}, t)$ are determined by the location and the extent of the target zone, whereas the temporal specification allows some degree of freedom. Typically [3,11, 13,17], pulse-like, broadband signals are used in the forward step. Next, the recorded displacements are time-reversed and broadcast from the mirror. This is the time-reversal step (*TR step*). In practice, both steps will be performed experimentally. In this article, we perform these steps computationally. Thus, the surrogate computational procedure for studying the TR method requires obtaining the solution of Eq. (1) twice, sequentially, with different initial and boundary conditions. The details of the numerical procedure are given below.

The forward step. We place the time-reversal mirror (sensors) on part of the boundary ($\Gamma_{\text{load}} \subset \partial\Omega_{\text{reg}}$), and fix the displacement on the rest of the boundary ($\Gamma_{\text{fix}} = \partial\Omega_{\text{reg}} \setminus \Gamma_{\text{load}}$). For the forward step, Γ_{load} is left traction free. Thus, the boundary conditions for the forward step are as follows:

$$\mathbf{T} = \mathbf{0}, \quad \mathbf{x} \in \Gamma_{\text{load}} \tag{2a}$$

$$\mathbf{u} = \mathbf{0}, \quad \mathbf{x} \in \Gamma_{\text{fix}} \tag{2b}$$

where $\mathbf{T}$ is the traction vector. We assume silent initial conditions, which imply

$$\mathbf{u}(\mathbf{x}, 0) = \mathbf{0}, \quad \mathbf{x} \in \Omega_{\text{reg}}, \tag{3a}$$

$$\dot{\mathbf{u}}(\mathbf{x}, 0) = \mathbf{0}, \quad \mathbf{x} \in \Omega_{\text{reg}}. \tag{3b}$$

We solve Eq. (1), driven by a prescribed source $\mathbf{f}(\mathbf{x}, t)$, subject to boundary conditions (2), and initial conditions (3), to obtain the displacement field $\mathbf{u}(\mathbf{x}, t)$ in Ω_{reg}. We record $\mathbf{u}(\mathbf{x}, t)$ on Γ_{load} (the time-reversal mirror).

The time-reversal step. To distinguish between the solution of the TR step and that of the forward step, we denote the displacement field in the TR step by $\bar{\mathbf{u}}$. We assume that we recorded the displacement history on the TR mirror until time $t = T$. The governing equations for the TR step take the following form:

$$\mathbf{div}\,[\mu\,(\nabla\bar{\mathbf{u}} + \nabla\bar{\mathbf{u}}^{\intercal})] + \mathbf{div}\,[\lambda\ (\text{div}\,\bar{\mathbf{u}})\ \mathbf{I}] - \rho\ddot{\bar{\mathbf{u}}} + \mathbf{f}\,(\mathbf{x}, T - t) = \mathbf{0}, \quad \mathbf{x} \in \Omega_{\text{reg}}, \tag{4}$$

where the time-reversed body force term, $\mathbf{f}(\mathbf{x}, T-t)$, is now a *sink* term. The sink provides the evanescent wave information, which is not captured by the TR mirror due to the distance between the source/sink and the mirror. During the TR step, the sink term absorbs the incoming waves and ensures a silent displacement field for $t \geq T$ (consistent with the forward step's initial conditions). In the absence of the sink term, the waves refocus, pass through the refocusing location, and continue to excite the finite elastic domain (i.e., $\bar{\mathbf{u}}(\mathbf{x}, t > T) \neq 0$).

In the TR step, the boundary condition on Γ_{fix} remains unchanged, but the boundary condition on Γ_{load} changes to

$$\bar{\mathbf{u}}(\mathbf{x}, t) = \mathbf{u}(\mathbf{x}, T - t), \quad \mathbf{x} \in \Gamma_{\text{load}}, \tag{5}$$

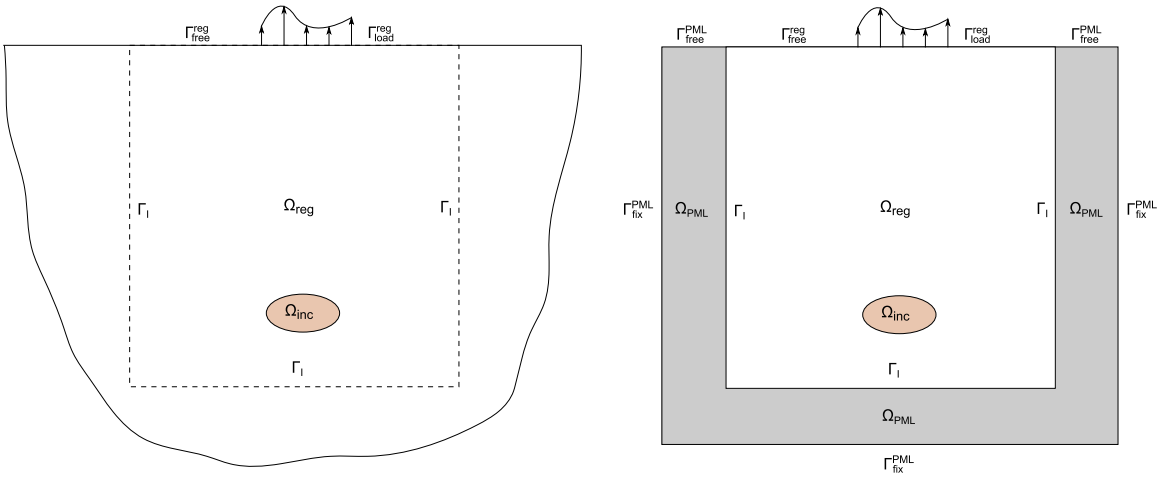

Fig. 2. A semi-infinite, heterogeneous, isotropic, elastic domain containing a target inclusion and the corresponding computational model.

where $\mathbf{u}(\mathbf{x}, T-t)$ is the time-reversed version of the displacement signal during the forward step. Note that enforcing a time-dependent, Dirichlet-type condition on the boundary of a heterogeneous, elastic domain is difficult to achieve in practice. At the end of the forward step ($t = T$), there exists a non-zero displacement field $\mathbf{u}(\mathbf{x}, T)$ in Ω_{reg}. This field acts as the initial condition in the TR step, i.e.,

$$\bar{\mathbf{u}}(\mathbf{x}, 0) = \mathbf{u}(\mathbf{x}, T), \quad \mathbf{x} \in \Omega_{\text{reg}}, \tag{6a}$$

$$\dot{\bar{\mathbf{u}}}(\mathbf{x}, 0) = -\dot{\mathbf{u}}(\mathbf{x}, T), \quad \mathbf{x} \in \Omega_{\text{reg}}. \tag{6b}$$

Once again, we note that it is difficult to enforce this non-zero initial condition in the domain of interest while performing the TR step in practice. Thus, the displacement field obtained by solving equation (4) with boundary condition (5) and initial conditions (6), corresponds to an ideal refocusing application by the time-reversal method in a finite, heterogeneous, elastic, isotropic domain. Formulation of a practically implementable version of the TR method for semi-infinite media necessitates a departure from the ideal case. In the next section, we discuss the TR method for *semi-infinite*, heterogeneous, elastic, isotropic media.

2.1.2. *The time-reversal method for semi-infinite, elastic domains*

Consider a semi-infinite, heterogeneous, elastic, isotropic domain of interest Ω_{reg} containing a target inclusion Ω_{inc} (Fig. 2). In order to obtain a finite computational domain, we truncate Ω_{reg} at Γ_{l}. Note that the displacement along the boundary Γ_{l} is not equal to zero. To achieve a physically faithful simulation of the wave propagation in our finite numerical model, we attach PML buffer zones (Ω_{PML}) to Ω_{reg} along Γ_{l}. The PML buffers ensure that the waves crossing the boundary Γ_{l} do so with negligible reflections. The governing equations in Ω_{PML} are given by [24]:

$$\mathbf{div}\left(\dot{\mathbf{S}}^{\intercal}\tilde{\Lambda}_e + \mathbf{S}^{\intercal}\tilde{\Lambda}_p\right) - \rho\left(\mathsf{a}\ddot{\bar{\mathbf{u}}} + \mathsf{b}\dot{\bar{\mathbf{u}}} + \mathsf{c}\bar{\mathbf{u}}\right) = \mathbf{0}, \quad \mathbf{x} \in \Omega_{\text{PML}}, \tag{7a}$$

$$\mathcal{D} : \left(\mathsf{a}\ddot{\mathbf{S}} + \mathsf{b}\dot{\mathbf{S}} + \mathsf{c}\dot{\mathbf{S}}\right) - \frac{1}{2}\left[(\nabla\bar{\mathbf{u}})\,\tilde{\Lambda}_p + \tilde{\Lambda}_p(\nabla\bar{\mathbf{u}})^{\intercal} + \left(\nabla\dot{\bar{\mathbf{u}}}\right)\tilde{\Lambda}_e + \tilde{\Lambda}_e(\nabla\dot{\bar{\mathbf{u}}})^{\intercal}\right] = \mathbf{0}, \quad \mathbf{x} \in \Omega_{\text{PML}}, \tag{7b}$$

where $\mathbf{S}(\mathbf{x}, t)$ is the stress history tensor, a colon (:) represents tensor inner product, $\mathcal{D}$ is the compliance tensor, $\tilde{\Lambda}_e$ and $\tilde{\Lambda}_p$ are components of the stretching tensor, and a, b, c are coefficients defining coordinate stretching in the PML region [24]. We have written Eqs. (7a) and (7b) for the TR step. We remark that the same equations govern the wave propagation in the forward step. Recall that in the forward step, the waves emitted by a source placed in the target (Ω_{inc}) are recorded by the mirror. In our computational model, and indeed, in a field experiment, we can place the mirror only on the free (ground) surface ($\Gamma^{\text{reg}}_{\text{load}}$). The remainder of the top boundary is traction free ($\Gamma^{\text{reg}}_{\text{free}}$). Note that in contrast to the case of finite, elastic domains, here, most of the wave energy emitted by the source placed in Ω_{inc} escapes Ω_{reg} without reaching the mirror.

Next, we discuss various points of departure from the ideal case described in Section 2.1.1, in an attempt to assess computationally the ramifications to the wave energy delivery of an *imperfectly-implemented* TR, since physical limitations prohibit the implementation of ideal TR conditions in the field.

Firstly, in practice, one cannot induce non-zero initial conditions (6) in the semi-infinite domain of interest.[2] Hence, we use silent initial conditions in our numerical simulations.

[2] It is not physically possible to impose any initial conditions to a volume that is part of the earth.

Secondly, due to equipment limitations, it is difficult/impossible to enforce a time-variant Dirichlet type boundary condition on the ground surface. Therefore, we use a traction boundary condition in the TR step, i.e., we use $\mathbf{T}(\mathbf{x}, t) = \mathbf{u}(\mathbf{x}, T - t)$ on $\Gamma^{\text{reg}}_{\text{load}}$,[3] instead of $\bar{\mathbf{u}}(\mathbf{x}, t) = \mathbf{u}(\mathbf{x}, T - t)$. We mention that Fink et al. [13] studied the effect of applying a Dirichlet boundary condition as a Neumann boundary condition in acoustics, and their analysis showed that refocusing can still be achieved.

Thirdly, a field implementation of the sink term would require a probe, acting initially as a source, to be inserted at the location of the target. During the TR step, the source should be time-reversed, thus creating the sink. However, for a higher energy yield at the target, the mirror data are amplified, which means that to maintain problem coherency, the probe/source, now acting as a sink, must also be amplified. Typically, the probe/source does not have amplitude agility to accommodate amplification (one cannot drive/install a strong motion actuator in an often deeply situated underground target region). Thus, in the context of the problem at hand, a physical realization of the sink is impossible. Therefore, we omit the sink term from our numerical simulations in order to assess computationally the effect of its omission because of the aforementioned physical limitations. As discussed earlier, this will not ensure the silent *final* condition during the TR step. But since we are interested in delivering wave energy to the target, rather than localizing or detecting the source accurately, a very sharp, localized refocus with silent pre- and post-focus behavior is not a necessity. In fact, the non-zero final displacements may add more wave energy to the target.

The complete initial and boundary value problem statement for the TR step, reflecting the discussed modifications when compared with the finite-domain ideal setting of Section 2.1.1, include the PML equations (7a) and (7b), as well as:

$$\mathbf{div}\,[\mu\,(\nabla\bar{\mathbf{u}} + \nabla\bar{\mathbf{u}}^{\mathsf{T}})] + \mathbf{div}\,[\lambda\ (\text{div}\ \bar{\mathbf{u}})\ \mathbf{I}] - \rho\ddot{\bar{\mathbf{u}}} = \mathbf{0}, \quad \mathbf{x} \in \Omega_{\text{reg}}, \tag{8}$$

with

$$\begin{aligned}
&\mathbf{T}(\mathbf{x}, t) = \mathbf{u}(\mathbf{x}, T - t), && \mathbf{x} \in \Gamma^{\text{reg}}_{\text{load}},\\
&\mathbf{T}(\mathbf{x}, t) = \mathbf{0}, && \mathbf{x} \in \Gamma^{\text{reg}}_{\text{free}} \cup \Gamma^{\text{PML}}_{\text{free}},\\
&\bar{\mathbf{u}}(\mathbf{x}, t) = \mathbf{0}, && \mathbf{x} \in \Gamma^{\text{PML}}_{\text{fix}},\\
&\bar{\mathbf{u}}(\mathbf{x}, 0) = \mathbf{0}, && \mathbf{x} \in \Omega,\\
&\dot{\bar{\mathbf{u}}}(\mathbf{x}, 0) = \mathbf{0}, && \mathbf{x} \in \Omega.
\end{aligned} \tag{9}$$

We solve the governing equations for the forward and the TR steps using the finite element method. To this end, we cast the governing equations in their weak form. We, then, introduce spatial discretization via piecewise continuous shape functions to arrive at the following semi-discrete form:

$$\mathbf{M}\ddot{\mathbf{d}} + \mathbf{C}\dot{\mathbf{d}} + \mathbf{K}\mathbf{d} = \mathbf{F}, \tag{10}$$

$$\mathbf{d} = [\mathbf{u}_{\text{inc}}\ \ \mathbf{u}\ \ \mathbf{u}_{\text{PML}}\ \mathbf{S}]^{\mathsf{T}}, \tag{11}$$

$$\mathbf{F} = [\mathbf{F}_{\text{inc}}\ \ \mathbf{F}_{\text{reg}}\ \ \mathbf{0}\ \mathbf{0}]^{\mathsf{T}}, \tag{12}$$

where $\mathbf{M}$, $\mathbf{C}$, and $\mathbf{K}$ are, the global mass, damping, and stiffness matrices, respectively, $\mathbf{d}$ is the vector of unknown displacements (everywhere) and stress histories (PML only), and $\mathbf{F}$ is the force vector. $\mathbf{u}_{\text{inc}}$, $\mathbf{u}$, $\mathbf{u}_{\text{PML}}$, and $\mathbf{S}$ denote vectors of nodal values of displacements ($\bar{\mathbf{u}}$ in Ω_{inc}, Ω_{reg}, and Ω_{PML}, respectively) and stress histories ($\mathbf{S}$ in Ω_{PML}). Note that $\mathbf{F}_{\text{inc}} \neq \mathbf{0}$, $\mathbf{F}_{\text{reg}} = \mathbf{0}$ for the forward step, and $\mathbf{F}_{\text{inc}} = \mathbf{0}$, $\mathbf{F}_{\text{reg}} \neq \mathbf{0}$ for the TR step. Further details of the finite element formulation, as well as the element and global matrices can be found in [19,24]. We discretize the temporal dimension using a timestep Δt. We define the vector $\mathbf{d}_i = \mathbf{d}$, at time $t = i\Delta t$. The equation of motion of the spatio-temporally discretized system at time $t = (i+1)\Delta t$ can be written as,

$$\mathbf{M}\ddot{\mathbf{d}}_{i+1} + \mathbf{C}\dot{\mathbf{d}}_{i+1} + \mathbf{K}\mathbf{d}_{i+1} = \mathbf{F}_{i+1}. \tag{13}$$

Note that Eqs. (13) represent the spatio-temporally discretized version of the governing partial differential equations (8), (7a) and (7b). We use Newmark's time integration scheme, with silent initial conditions ($\mathbf{d}_0 = \dot{\mathbf{d}}_0 = \mathbf{0}$), to integrate Eq. (13) in time. Thus, we can now perform the forward and TR steps using this computational model of the wave propagation in the semi-infinite medium of interest, accounting for the non-ideal TR conditions discussed earlier. In the next section, we turn our attention to the other wave-energy-focusing methodology, viz., the inverse-source approach.

2.2. The inverse-source method

The IS method is an optimization-based approach aimed at computing the optimal wave source characteristics, where optimality is defined based on maximization of a motion metric of the target inclusion. Here, we provide a brief outline of the inversion methodology; a detailed discussion can be found in [19].

[3] The equation implies that the time-domain trace of the displacements is used to apply tractions with, however, a suitable adjustment to the amplitude and units.

2.2.1. The forward problem

Consider the semi-infinite, heterogeneous, elastic, isotropic domain of interest Ω_{reg} containing a target inclusion Ω_{inc} (Fig. 2). Let $\mathbf{u}_{\text{inc}}(\mathbf{x}, t)$ represent the displacement field in the target inclusion Ω_{inc}, and let $\mathbf{u}(\mathbf{x}, t)$ denote the displacement in the rest of the domain $\Omega_{\text{reg}} \cup \Omega_{\text{PML}}$. The wave motion in Ω_{reg} is initiated by traction forces $\mathbf{T}(\mathbf{x}, t)$ applied on $\Gamma^{\text{reg}}_{\text{load}}$. The traction $\mathbf{T}(\mathbf{x}, t)$ forces consist of contributions from n_s sources. The ith source consists of a spatial $\boldsymbol{\theta}_i(\mathbf{x})$ and a temporal $g_i(t)$ component. $\boldsymbol{\theta}_i$ is further decomposed into the x_1-directional component $\theta_{i1}(\mathbf{x})$ and the x_2-directional component $\theta_{i2}(\mathbf{x})$. Thus,

$$\mathbf{T}(\mathbf{x}, t) = \sum_{i=1}^{n_s} \begin{bmatrix} \boldsymbol{\theta}_{i1}(\mathbf{x}) \\ \boldsymbol{\theta}_{i2}(\mathbf{x}) \end{bmatrix} g_i(t). \tag{14}$$

The *continuous* form of the equations governing the wave propagation in the semi-infinite domain of interest ($\Omega = \Omega_{\text{reg}} \cup \Omega_{\text{inc}} \cup \Omega_{\text{PML}}$) is given by:

$$\mathbf{div}\left[\mu\left(\nabla\mathbf{u}_{\text{inc}} + \nabla\mathbf{u}_{\text{inc}}^{\intercal}\right)\right] + \mathbf{div}\left[\lambda\ (\text{div}\ \mathbf{u}_{\text{inc}})\ \mathbf{I}\right] - \rho\ddot{\mathbf{u}}_{\text{inc}} = \mathbf{0}, \quad \mathbf{x} \in \Omega_{\text{inc}}, \tag{15}$$

$$\mathbf{div}\left[\mu\left(\nabla\mathbf{u} + \nabla\mathbf{u}^{\intercal}\right)\right] + \mathbf{div}\left[\lambda\ (\text{div}\ \mathbf{u})\ \mathbf{I}\right] - \rho\ddot{\mathbf{u}} = \mathbf{0}, \quad \mathbf{x} \in \Omega \setminus \Omega_{\text{inc}}, \tag{16}$$

$$\mathbf{div}\left(\dot{\mathbf{S}}^{\intercal}\tilde{\Lambda}_e + \mathbf{S}^{\intercal}\tilde{\Lambda}_p\right) - \rho\left(\mathrm{a}\ddot{\mathbf{u}} + \mathrm{b}\dot{\mathbf{u}} + \mathrm{c}\mathbf{u}\right) = \mathbf{0}, \quad \mathbf{x} \in \Omega_{\text{PML}}, \tag{7a}$$

$$\mathcal{D} : \left(\mathrm{a}\ddot{\mathbf{S}} + \mathrm{b}\dot{\mathbf{S}} + \mathrm{c}\dot{\mathbf{S}}\right) - \frac{1}{2}\left[(\nabla\mathbf{u})\,\tilde{\Lambda}_p + \tilde{\Lambda}_p(\nabla\mathbf{u})^{\intercal} + (\nabla\dot{\mathbf{u}})\,\tilde{\Lambda}_e + \tilde{\Lambda}_e(\nabla\dot{\mathbf{u}})^{\intercal}\right] = \mathbf{0}, \quad \mathbf{x} \in \Omega_{\text{PML}}. \tag{7b}$$

The governing equations are subjected to additional boundary, interface, and initial conditions that have been suppressed for brevity. We use the finite element method to resolve the forward problem. After *spatio-temporal discretization* of the governing PDEs, we arrive at a semi-discrete form similar to (13). Here too, we use Newmark's time-marching procedure to integrate (13) in time. We remark that the Newmark's time integration scheme is equivalent to solving a system of equations given by

$$\boldsymbol{Q}\boldsymbol{u} = \boldsymbol{f}, \tag{17}$$

where,

$$\boldsymbol{u} = [\ddot{\mathbf{d}}_0\ \dot{\mathbf{d}}_0\ \mathbf{d}_0\ \ddot{\mathbf{d}}_1\ \dot{\mathbf{d}}_1\ \mathbf{d}_1\ \cdots\ \ddot{\mathbf{d}}_N\ \dot{\mathbf{d}}_N\ \mathbf{d}_N\ ]^{\intercal}, \tag{18}$$

$$\boldsymbol{f} = [\mathbf{F}_0\ \dot{\mathbf{d}}_0\ \mathbf{d}_0\ \mathbf{F}_1\ \mathbf{0}\ \mathbf{0}\ \cdots\ \mathbf{F}_N\ \mathbf{0}\ \mathbf{0}]^{\intercal}, \tag{19}$$

and $\mathbf{Q}$ is defined in [19]. The spatio-temporally discretized system of equations (17) will be used to formulate the inverse-source problem.

In the inverse-source formulation, the surface loads are treated as unknowns. The load descriptors are updated iteratively during the inversion process. This calls for parameterization of the spatio-temporal characteristics of the loads defined in Eq. (14). We parameterize the (unknown) time signal(s) using piecewise quadratic Lagrange polynomials $\tau_j(t)$ whose temporal nodal values are denoted by ξ_{ij}. This allows us to express $g_i(t)$ as

$$g_i(t) = \sum_{j=1}^{n_f} \xi_{ij}\tau_j(t), \tag{20}$$

where, n_f is the total number of Lagrange polynomials. The spatial variation of the ith load on Γ_{load} is captured by θ_{iK}, where subscript K describes the direction in which the load acts. In this article, we use horizontally polarized loads that vary like a Gaussian function on the loaded boundary ($x_2 = 0$). Thus, the spatial variation of the i-th surface load, centered at η_i, is given by,

$$\theta_{i1}(x_1, 0) = -\exp\left[\frac{-(x_1 - \eta_i)^2}{1.25}\right]. \tag{21}$$

2.2.2. The inverse problem

Next, we discuss the inverse-source formulation using the *discretize-then-optimize* (DTO) approach (in lieu of the classical *optimize-then-discretize* (OTD) approach). The inverse-source problem aims at maximizing a motion metric of the target inclusion by seeking optimal time signals and locations for the surface tractions. For the DTO approach we select the following objective functional (whose minimization is tantamount to maximization of the velocity field in the target inclusion):

$$\mathcal{L}_d = \frac{1}{\int_0^T \rho_{\text{inc}}\dot{\mathbf{u}}_{\text{inc}}^{\intercal}\dot{\mathbf{u}}_{\text{inc}}dt} \simeq \frac{1}{\rho_{\text{inc}}\boldsymbol{u}^{\intercal}\boldsymbol{B}_{u_{\text{inc}}}\boldsymbol{u}}, \tag{22}$$

where, $\boldsymbol{B}_{u_{\text{inc}}}$ is a block diagonal matrix with $\Delta t \boldsymbol{B}_{\text{i}}$ on its diagonals; $\boldsymbol{B}_{\text{i}}$ are square matrices that are zero everywhere except on diagonals that correspond to the $\dot{\mathbf{u}}_{\text{inc}}$ degrees of freedom. We note that the choice of the velocity field in the target as the performance metric is due to one of the driving applications (EOR), and the associated laboratory experiments that support such a choice. Specifically, for EOR purposes the goal is to dislodge oil ganglia (or, more generally, trapped particles) by overcoming capillary forces. The conducted laboratory experiments promote the notion of vibrating the solid matrix to facilitate the *shaking out* of the ganglia [25–29]. Maximization of other metrics may be important for different applications. In such a case, the IS approach would simply require a different objective functional to accommodate the new metric, but the overall approach will still remain largely unchanged.

We superimpose the governing equations (17), weighted by the discrete Lagrange multipliers $\boldsymbol{p}$, on the objective functional to obtain the discrete Lagrangian, $\mathcal{A}_d$, which is to be minimized. Thus, the constrained minimization problem can now be stated as,

$$\min_{\boldsymbol{f}} \ \mathcal{A}_d(\boldsymbol{u}, \boldsymbol{p}, \boldsymbol{f}), \ \text{or,} \ \min_{\boldsymbol{f}} \ \mathcal{L}_d - \boldsymbol{p}^{\mathsf{T}}(\boldsymbol{Q}\boldsymbol{u} - \boldsymbol{f}), \tag{23}$$

where,

$$\boldsymbol{p} = [\ddot{\boldsymbol{\lambda}}_0 \ \dot{\boldsymbol{\lambda}}_0 \ \boldsymbol{\lambda}_0 \ \ddot{\boldsymbol{\lambda}}_1 \ \dot{\boldsymbol{\lambda}}_1 \ \boldsymbol{\lambda}_1 \ \cdots \ \ddot{\boldsymbol{\lambda}}_N \ \dot{\boldsymbol{\lambda}}_N \ \boldsymbol{\lambda}_N \ ]^{\mathsf{T}}, \tag{24}$$

$$\boldsymbol{\lambda} = [\boldsymbol{\lambda}_{u_{\text{inc}}} \,|\, \boldsymbol{\lambda}_u \,|\, \boldsymbol{\lambda}_{u_{\text{PML}}} \boldsymbol{\lambda}_S]^{\mathsf{T}}, \quad \boldsymbol{\lambda}_i = \boldsymbol{\lambda}, \ \text{at } t = i\Delta t. \tag{25}$$

The first-order optimality conditions are now obtained by taking derivatives of $\mathcal{A}_d$ with respect to $\boldsymbol{u}, \boldsymbol{p}$, and the force-parameters ξ, η.

2.3. The first condition—state problem

$$\frac{\partial \mathcal{A}_d}{\partial \boldsymbol{p}} = \boldsymbol{0} \Longrightarrow \boldsymbol{Q}\boldsymbol{u} = \boldsymbol{f}, \tag{26}$$

which is the *forward* problem, given by Eq. (17).

2.4. The second condition—adjoint problem

$$\frac{\partial \mathcal{A}_d}{\partial \boldsymbol{u}} = \boldsymbol{0} \Longrightarrow \boldsymbol{Q}^{\mathsf{T}}\boldsymbol{p} = \frac{-2\boldsymbol{B}_{u_{\text{inc}}}\boldsymbol{u}}{\rho_{\text{inc}} \ (\boldsymbol{u}^{\mathsf{T}}\boldsymbol{B}_{u_{\text{inc}}}\boldsymbol{u})^2}. \tag{27}$$

Eq. (27) represents the *adjoint* problem associated with the inverse problem of interest. Since the adjoint problem involves the transpose of $\boldsymbol{Q}$, we solve it by marching backwards in time. The adjoint problem of the DTO approach is driven by prescription of the velocity-like adjoint variables in the target inclusion at each time step.

2.5. The third condition—control problem(s)

Time signal optimization. For a load acting in the x_p direction, we update each element, ξ_{mn}, of the control parameter vector $\boldsymbol{\xi}$, using:

$$\frac{\partial \mathcal{A}_d}{\partial \xi_{mn}} = \sum_{k=0}^{N} \tau_n(k\Delta t) \, \ddot{\boldsymbol{\lambda}}^{\mathsf{T}}_{k,\text{load}} \int_{\Gamma_{\text{load}}} \boldsymbol{\theta}_{mp}(\mathbf{x}) \boldsymbol{\Phi} \, d\Gamma. \tag{28}$$

Load location optimization. For a load acting in the x_p direction, we update each element, η_m, of the control parameter vector $\boldsymbol{\eta}$, using:

$$\frac{\partial \mathcal{A}_d}{\partial \eta_m} = \sum_{k=0}^{N} \left[\left(\sum_{j=1}^{n_f} \xi_{mj} \tau_j(k\Delta t) \right) \ddot{\boldsymbol{\lambda}}^{\mathsf{T}}_{k,\text{load}} \int_{\Gamma_{\text{load}}} \frac{\partial \boldsymbol{\theta}_{mp}(\mathbf{x})}{\partial \eta_m} \boldsymbol{\Phi} \, d\Gamma \right]. \tag{29}$$

We start the inversion process with an initial guess for the source characteristics. We, then, solve the forward problem, compute the objective functional ($\mathcal{L}_d$), and obtain the velocity field in the target ($\dot{\mathbf{u}}_{\text{inc}}$). We use the values of $\mathcal{L}_d$ and $\dot{\mathbf{u}}_{\text{inc}}$ to compute the velocity-like adjoint variables in the target inclusion, and solve the adjoint problem. Solution of the adjoint problem yields values of the acceleration-like adjoint variables on the loaded boundary ($\ddot{\boldsymbol{\lambda}}_{k,\text{load}}$). We, then, use Eq. (28) and/or (29) to compute the discrete reduced gradients. We update the source characteristics using the conjugate gradient method, and follow an iterative inversion procedure until convergence is reached. Upon convergence, the inversion algorithm yields

Table 1
Material properties of the layers and the inclusion in the geological formation model.

	ρ (kg/m^3)	ν	E (GPa)
Layer 1	2200	0.2	1.5
Layer 2	2200	0.2	2.5
Layer 3	2200	0.2	3.5
Layer 4	2200	0.2	4.5
Inclusion	2200	0.2	1.0

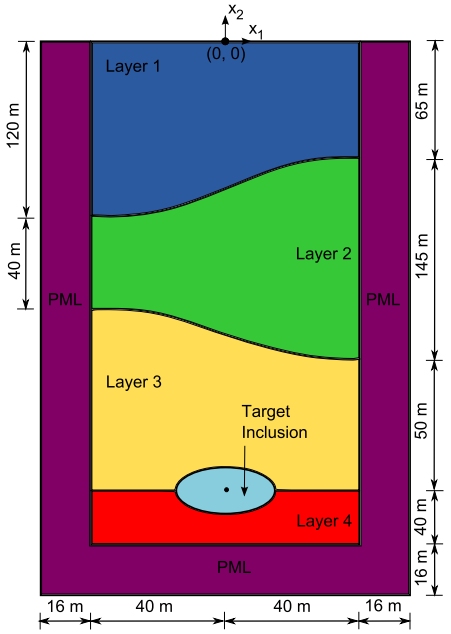

Fig. 3. Geological formation model.

the source characteristics that minimize $\mathcal{L}_d$, which is tantamount to maximizing the velocity field in the target inclusion. Additional details of the inverse-source algorithm can be found in [19].

We remark that the objective functional $\mathcal{A}_d$ is defined using the reciprocal of the square of the velocity field in the target zone, augmented by the side-imposition of the governing physics, per Eq. (23). Both terms in Eq. (23) are written in their discrete form. The functional form $\mathcal{A}_d$ is not necessarily convex, and convergence is not guaranteed. However, in our experience: (a) the methodology has never failed to converge (to a local or a global minimum), whether executed as simultaneous space location and time signal optimization, or in sequential mode; (b) when we fix the source location, and optimize with respect to the time signal only, we assert that the optimizer converges to the global minimum, since in these cases frequency sweeps have provided confirmation that the correct frequency content has been attained.

3. Numerical experiments

In this section, we test the TR and IS methodologies by conducting numerical experiments on a synthetically created, two-dimensional, layered, elastic, isotropic geological formation model (Fig. 3). The formation model consists of four layers, and an elliptic inclusion sandwiched between the third and fourth layers. The major and minor semi-axes of the elliptic inclusion are, respectively, 15 m and 7.5 m long. The top boundary ($x_2 = 0$) represents the ground surface, where we apply loads and record displacements (the TR mirror). Material properties of the layers are summarized in Table 1. Note that in Table 1, ρ, ν and E are mass density, Poisson's ratio and Young's modulus respectively.

In [19], Karve et al. used this model to exercise the inversion algorithm that computes the optimal spatio-temporal characteristics of surface wave sources. Here, we compare the performance of the wave sources designed in [19], and those resulting from the TR approach. To this end, we first define the following motion metrics that allow quantitative assessment of wave energy delivery:

1. The mechanical energy expended by the traction forces acting on the ground surface can be estimated by computing,

$$\mathrm{E}_{\mathrm{input}} = \int_0^T \int_{\Gamma_{\mathrm{load}}^{\mathrm{reg}}} \mathbf{T}(\mathbf{x}, t)\, d\bar{\mathbf{u}}(\mathbf{x}, t) = \int_0^T \mathbf{F}^{\mathsf{T}}(t)\dot{\mathbf{d}}(t)\, dt, \tag{30}$$

where **F** is the global force vector, and **d** is the vector of nodal displacements and stress histories. The SI units of E_{input} are J/m. We remark that the energy expended by the mechanical assembly used to apply the surface loads (e.g., Vibroseis) depends on the mechanical efficiency of its parts (e.g., hydraulic press, IC engine, etc.), and is not the same as E_{input}.

2. If $\dot{\mathbf{u}}(\mathbf{x}, t)$ is the velocity vector at a computational node, then the average kinetic energy at the computational node, over the entire simulation time is given by:

$$KE_{TA}(\mathbf{x}) = \frac{1}{2T}\int_0^T \dot{\mathbf{u}}(\mathbf{x}, t)\rho\dot{\mathbf{u}}(\mathbf{x}, t)\, dt. \tag{31}$$

The SI units of $KE_{TA}(\mathbf{x})$ are J/m^3. We use plots of $KE_{TA}(\mathbf{x})$ for visually assessing the *silent* and *excited* regions in the formation.

3. The *instantaneous* kinetic energy of the target inclusion at time t can be computed as,

$$KE_{inc}(t) = \frac{1}{2}\int_{\Omega_{inc}} \dot{\mathbf{u}}_{inc}(\mathbf{x}, t)\rho_{inc}\dot{\mathbf{u}}_{inc}(\mathbf{x}, t)\, d\Omega \simeq \frac{1}{2}\dot{\mathbf{u}}_{inc}^T(t)\mathbf{M}_{inc}\dot{\mathbf{u}}_{inc}(t), \tag{32}$$

where $\mathbf{M}_{inc}$ is the mass matrix of the inclusion [19], and $\dot{\mathbf{u}}_{inc}$ is the nodal velocity vector for the target inclusion [19]. The SI units of $KE_{inc}(t)$ are J/m.

4. We define the time-averaged kinetic energy of the inclusion as,

$$KE_{inc}^{avg} = \frac{1}{T_2 - T_1}\int_{T_1}^{T_2} KE_{inc}(t)\, dt. \tag{33}$$

The values of T_1 and T_2 can be obtained by carefully observing the time history of the kinetic energy of the inclusion ($KE_{inc}(t)$). T_1 is the first moment at which the plot of $KE_{inc}(t)$ shows a sharp rise, whereas T_2 is the last moment in time at which the plot of $KE_{inc}(t)$ shows a sudden fall. Thus, $(T_2 - T_1)$ denotes (approximately) the average duration for which the stress wave stimulation was applied, and the time-averaged kinetic energy (KE_{inc}^{avg}) measures, in J/m, the average amount of kinetic energy delivered to the inclusion over the time period for which the wave stimulation is applied.

Furthermore, we use the ratio of time-averaged kinetic energy and the input energy (KE_{inc}^{avg}/E_{input}) as a measure of the efficiency of the wave energy delivery process. Next, we conduct numerical experiments to test the utility of the TR and IS methodologies.

3.1. Numerical experiment 1

We begin our numerical experimentation by considering two important aspects of time-reversal for geophysical applications in semi-infinite media: (a) the number of sensors and sources used for TR, and (b) the time signal (frequency content) used in the forward step of TR. In practice, it is not feasible to cover the ground surface by sensors and motion actuators. Thus, it is important to evaluate the effect the number of sensors/sources has on the quality (contrast) and intensity (magnitude) of the refocus. In this experiment, we vary the number of the uniformly distributed sensors installed on the (80 m-wide) top boundary ($x_2 = 0$) of the geological formation model, and study the effect of mirror density on refocusing. Specifically, we place two adjacent sensors (and sources) either 0.5 m apart (*full mirror*), or 2.0 m apart (*quarter density mirror*). Thus, although the *full* and *quarter* density mirrors use different sensor spacing, they cover the entire 80 m-wide top boundary, i.e., the size of the mirror remains the same for both cases. Another key aspect of the TR method is the choice of the time signal used in the forward step. Although the governing physics allows refocus irrespective of the frequency content of the forward step signal, the amount of energy delivered to the target may be significantly different for different forward step signals. Here, we experiment with two types of signals in the forward step: (a) a series of rectangular pulses forming a comb-like signal (continuous wave like signal with narrow frequency support), and (b) a modified Ricker pulse (a pulse-like signal with wide frequency support). Thus, in this numerical experiment, for each of the forward step signals mentioned above, we evaluate the effect of mirror density, and report on the quality and intensity of wave energy focusing.

3.1.1. A series of rectangular pulses (experiment 1A)

A typical wave energy focusing application (e.g., wave-based EOR) calls for a sustained stress wave stimulation of the target zone. Such stimulation can be delivered by designing the wave sources using a series of rectangular pulses in the forward step of the TR method, e.g., the comb-like signal depicted in Fig. 4(a). The frequency spectrum of the comb-like signal is shown in Fig. 4(b). It can be seen in Fig. 4(b) that the comb-like signal has three dominant frequencies — roughly 14 Hz, 28 Hz and 43 Hz. In the forward step, we apply a horizontal (x_1-directional) point load, whose magnitude is described by the comb-like signal, at the center of the target inclusion. We terminate the forward step simulation after 1 s ($T = 1$ s). The time-reversal mirror records the waves emitted by the point load; for example, Fig. 4(c) shows the horizontal displacement recorded at coordinates (0, 0). All the other surface sensors have their own displacement records. Fig. 4(d) shows the frequency spectrum of the displacement recorded at (0, 0). It can be seen in Fig. 4(d) that the heterogeneous elastic domain reduced the participation of two of the dominant frequencies of the input signal. Next, we time-reverse

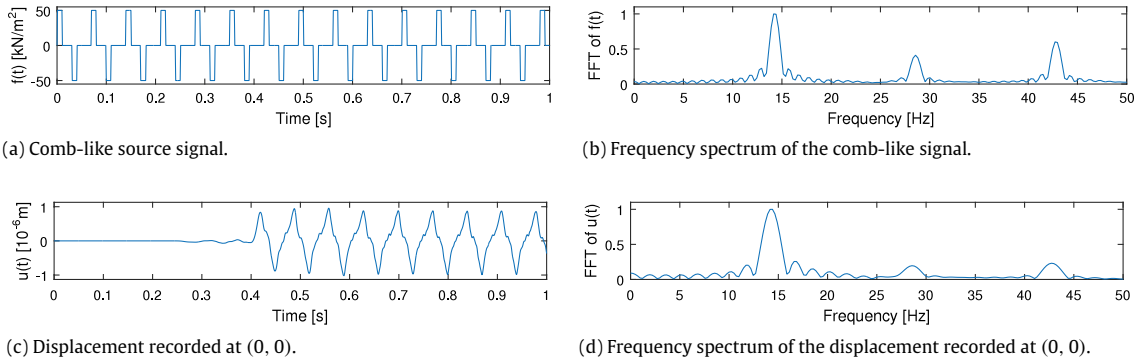

(a) Comb-like source signal.

(b) Frequency spectrum of the comb-like signal.

(c) Displacement recorded at (0, 0).

(d) Frequency spectrum of the displacement recorded at (0, 0).

Fig. 4. The source time signal and the recorded displacement (forward step)—experiment 1A.

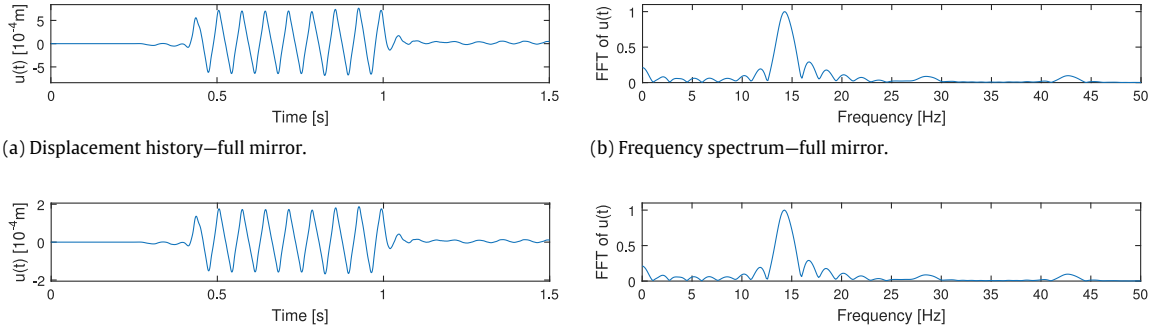

(a) Displacement history—full mirror.

(b) Frequency spectrum—full mirror.

(c) Displacement history—quarter density mirror.

(d) Frequency spectrum—quarter density mirror.

Fig. 5. Displacement histories and their frequency spectra for the TR step—experiment 1A.

Table 2
Motion metrics for experiment 1A.

	Full mirror	Quarter density mirror
KE_{inc}^{avg} [J/m]	4.2197×10^{2}	2.5424×10^{1}
E_{input} [J/m]	8.1094×10^{4}	4.9730×10^{3}
KE_{inc}^{avg}/E_{input}	5.2034×10^{-3}	5.1126×10^{-3}

the recorded signals (Fig. 4(c)) and apply horizontal point loads, whose temporal description is given by the time-reversed signals, at the respective sensor locations. Note that in the TR step we amplify the amplitude of the point loads so that the maximum amplitude is 50 kN/m. The rebroadcast waves refocus at the source location in the forward step, and stimulate the target inclusion. In order to allow the passage of waves from the computational domain, we extend the simulation time for the TR step to 1.5 s (as opposed to 1 s for the forward step). That is, the surface loads remain silent after 1 s, and we allow extra 0.5 s for the waves to evacuate the semi-infinite domain. The displacement histories at the center of the target inclusion for each mirror density case are depicted in Fig. 5(a) and (c), and their frequency spectra are shown in Fig. 5(b) and (d) respectively. The (horizontal) displacement histories differ only in magnitude, and hence, the (normalized) frequency spectra for the full and quarter density mirror cases are identical. Note that the displacement histories have a single dominant frequency of 14 Hz. Fig. 6 shows the plots of $KE_{inc}(t)$ for the two mirror densities. Similar to the displacement histories, the histories of KE_{inc} are identical in shape — the difference is in their magnitude. The plots of KE_{TA} for the entire domain are depicted in Fig. 7. The contrast between KE_{TA} values of the inclusion and its surroundings suggests a good quality refocus. The two figures are almost indistinguishable because their respective time-reversal mirrors have the same size. The mirror density affects the intensity of refocus, but not the quality of refocus — the scale bars on the right are different for the two figures.

The values of various motion metrics for the full and quarter mirror density cases are summarized in Table 2. It can be seen that the ratio of time-averaged kinetic energy of the inclusion to the input energy does not depend on mirror density. For the quarter density mirror case, both KE_{inc}^{avg} and E_{input} are reduced by a factor of $\frac{1}{16}$ as compared to those values for the full mirror density case. This observation agrees well with the experiments reported in [12,30,31], and provides a validation for our numerical surrogate procedure for the TR method. We conclude that for semi-infinite elastic media, reducing the number of sensors on time-reversal mirror only affects the energy intensity of refocus and not the quality of refocus.

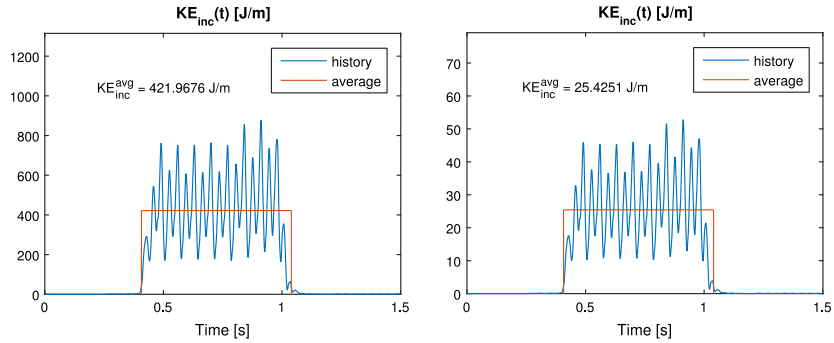

(a) Full mirror. (b) Quarter density mirror.

Fig. 6. Time history of the kinetic energy of the inclusion—experiment 1A.

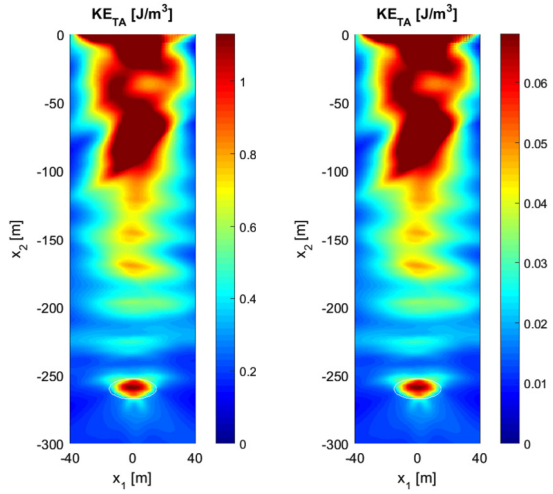

(a) Full mirror. (b) Quarter density mirror.

Fig. 7. $\mathrm{KE_{TA}}$ ($\mathrm{J/m^3}$) after the TR step—experiment 1A.

3.2. A modified Ricker pulse (experiment 1B)

In experiment 1A above, the comb-like source signal used in the forward step (Fig. 4(a)) was merely a guess. The comb-like signal had three dominant frequencies in its spectrum, and the forward step filtered two of them out. In the TR step, we rebroadcast the near-monochromatic signal and achieved a good quality refocus as seen in Fig. 7. Thus, the forward step acted as a filter and *selected* the frequencies that help illuminate the target inclusion. It has been reported [18,19] that the kinetic energy of target elastic inclusions embedded in layered, heterogeneous, semi-infinite elastic domains can be maximized if the sources operate at one of the *amplification* frequencies of the formation. The amplification frequency can be determined by conducting a frequency sweep.[4] Thus, if the amplification frequency of the target is present in the time signal of the forward step, then the displacements recorded by the TR mirror should show a bias. Typically, the amplification frequency of the target is not known *a priori*. Hence, a blindly chosen CW-like (narrow band) signal may not contain the amplification frequency in its spectrum. This is a key drawback of using CW-like signals in the forward step. Consequently, a broadband signal may be more suitable for use in the forward step. In this experiment, we explore this possibility by using a modified Ricker pulse as a candidate broadband signal. The equation defining the modified Ricker pulse is given by

$$f(t) = (1 - 2\pi^2(f_0 t - 1))^2 e^{-\pi^2(f_0 t-1)^2}, \tag{34}$$

where f_0 is the central frequency of the modified Ricker pulse. Here, we choose $f_0 = 25$ Hz (Fig. 8(a)). Karve et al. [19] conducted the frequency sweep for the geological formation model shown in Fig. 3, and reported that for horizontally

[4] In a frequency sweep, a numerical model of the governing wave physics is used to compute a predefined motion metric of the target for a range of monochromatic frequencies driving the sources. The frequency corresponding to the maximum value of the motion metric is termed the *amplification frequency* [18,19].

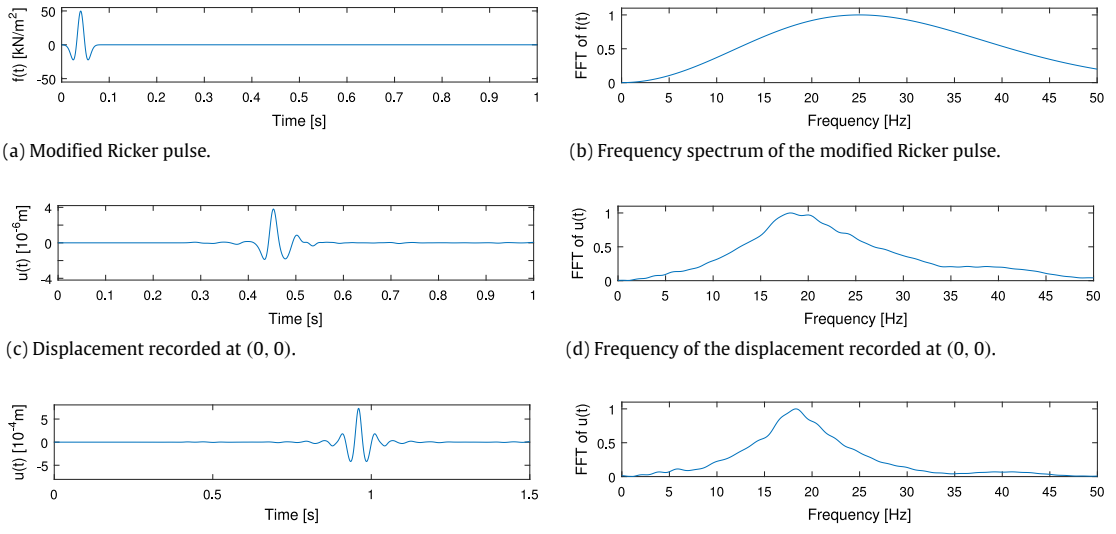

(a) Modified Ricker pulse.

(b) Frequency spectrum of the modified Ricker pulse.

(c) Displacement recorded at (0, 0).

(d) Frequency of the displacement recorded at (0, 0).

(e) Refocus displacement at the center of the target inclusion.

(f) Frequency spectrum of the refocus displacement.

Fig. 8. The source time signal, the recorded displacement, and the refocus displacement—experiment 1B.

Table 3
Motion metrics for experiments 1A and 1B.

	Full mirror	Quarter density mirror
KE_{inc}^{avg} [J/m]	2.6517×10^{2}	1.6084×10^{1}
E_{input} [J/m]	9.6943×10^{3}	5.9528×10^{2}
KE_{inc}^{avg}/E_{input} (modified Ricker)	2.7353×10^{-2}	2.7019×10^{-2}
KE_{inc}^{avg}/E_{input} (comb-like)	5.2034×10^{-3}	5.1126×10^{-3}

polarized surface loads the amplification frequency is (approximately) 18 Hz. It can be seen from Fig. 8(b) that the amplification frequency (18 Hz) is present in the spectrum of the forward step signal. We send the modified Ricker signal from the inclusion and record the displacements on the ground surface. A closer look at the frequency spectrum of the input signal (Fig. 8(b)) and that of the recorded displacement (Fig. 8(d)) reveals that the peak of the spectrum is shifted from 25 Hz to around 18 Hz. We time-reverse the recorded displacements and rebroadcast from their respective locations in the TR step. Fig. 8(e) shows the displacement history at the center of the inclusion in the TR step. It can be seen that the peak of the frequency spectrum of the TR displacement (Fig. 8(f)) is further sharpened. The bias towards the amplification frequency is clearly evident. The values of other motion metrics for the modified Ricker pulse as well as the comb-like signal are given in Table 3. The ratios of KE_{inc}^{avg} to E_{input} for the case of the modified Ricker pulse are about five times greater than those for the case of the comb-like signal. We conclude that a broadband signal (especially, a signal that contains the amplification frequency in its spectrum) enhances the ability of the TR process and increases the efficiency of wave energy delivery (Fig. 9).

3.3. Numerical experiment 2

In this experiment, we compare the performance of wave sources designed using the TR and the IS methodologies. Specifically, we compare the time-averaged kinetic energy (KE_{inc}^{avg}) and the efficiency (KE_{inc}^{avg}/E_{input}) of the energy delivery achieved by wave sources suggested by the two approaches. In [19], Karve et al. computed the optimal source time signals and source locations for three horizontally polarized loads applied on the boundary of the geological formation model (Fig. 3) using the IS approach. In the IS formulation [19], the source time signals and the source locations were optimized either simultaneously or sequentially. Here, we consider the three optimal source descriptions (named IS1, IS2, and IS3 in Table 4) reported in [19]. Their brief description is given below:

- Time signal optimization (case IS1)—the locations of the surface loads are guessed and only the time signals are optimized using the inversion algorithm.
- Sequential optimization (case IS2)—in the first step, the time signals are optimized without changing their locations. In the second step, the optimized time signals are kept unchanged and only the load locations are optimized.
- Simultaneous optimization (case IS3)—both the source time signals and the source locations are optimized simultaneously using the inversion framework.

The source time signals for the IS1, IS2, and IS3 cases are given in Figs. 10 and 11. The time histories of the kinetic energy of the inclusion, and the plots of KE_{TA} are given in Figs. 12 through 14.

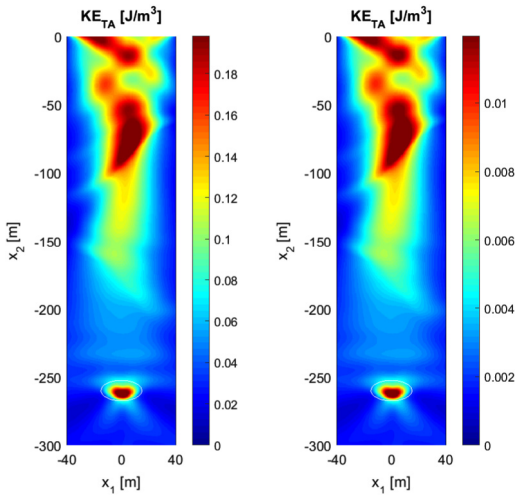

(a) Full mirror. (b) Quarter density mirror.

Fig. 9. KE_{TA} (J/m^3) after the TR step—experiment 1B.

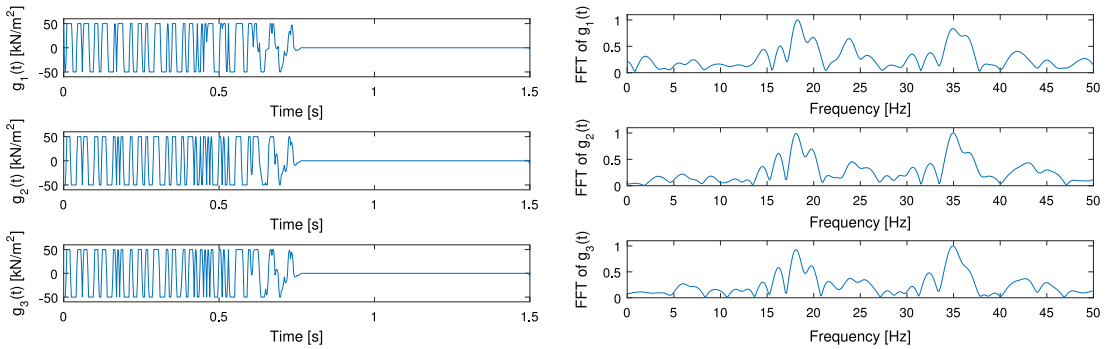

(a) Time signals. (b) Frequency spectra.

Fig. 10. IS1 and IS2—time signals and frequency spectra.

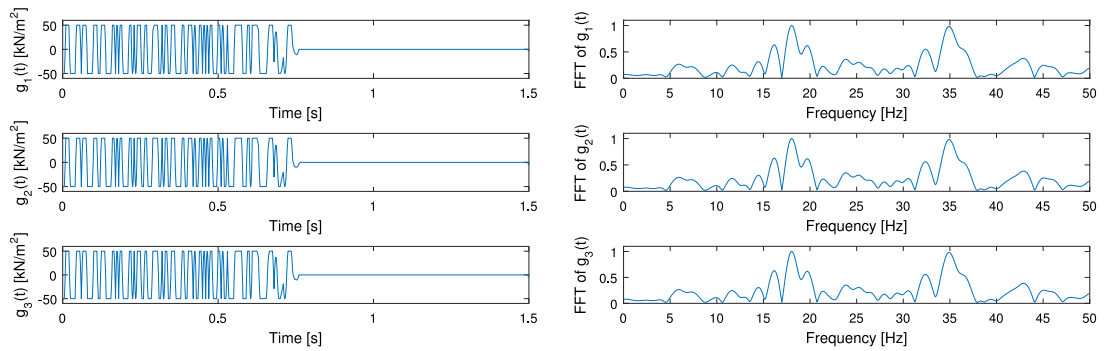

(a) Time signals at $(-20.04, 0)$ m, $(-19.16, 0)$ m, $(-19, 0)$ m respectively.

(b) Frequency spectra at $(-20.04, 0)$ m, $(-19.16, 0)$ m, $(-19, 0)$ m respectively.

Fig. 11. IS3—time signals and frequency spectra.

For the TR approach, we place the wave sources at the guessed or the optimal locations given by Karve et al. [19] (the third column of Table 4), but use the time signals computed using the TR method (cases TR1, TR2, and TR3 in Table 4). The key differences between the TR procedure followed in experiment 1 and that used in experiment 2 are given below:

- A uniform illumination of the target inclusion by a sufficiently strong wave field is essential for the success of geophysical applications. Accordingly, the inverse-source problem attempts maximization of the velocity field in the entire target

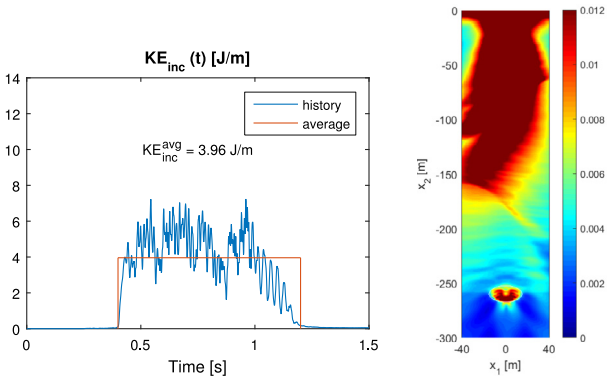

(a) History of KE_{inc}. (b) KE_{TA}.

Fig. 12. $KE_{inc}(t)$ and KE_{TA} after source time signal optimization (IS1).

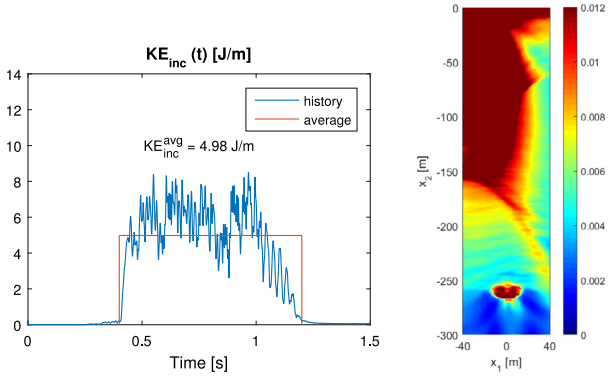

(a) History of KE_{inc}. (b) KE_{TA}.

Fig. 13. $KE_{inc}(t)$ and KE_{TA} after sequential source time signal and location optimization (IS2).

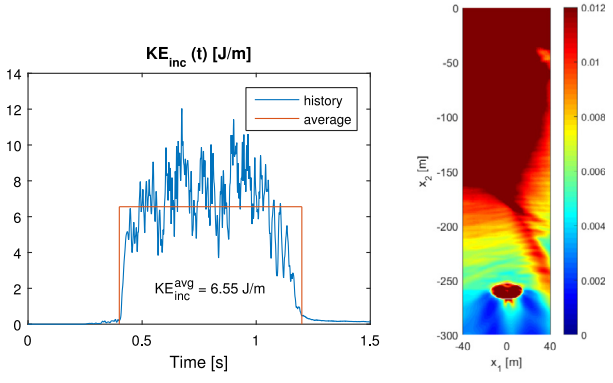

(a) History of KE_{inc}. (b) KE_{TA}.

Fig. 14. $KE_{inc}(t)$ and KE_{TA} after simultaneous source time signal and location optimization (IS3).

inclusion. In order to achieve a similar effect, here, we excite the entire inclusion rather than the center of the inclusion in the forward step. Thus, the displacement recorded at the mirror results from the superposition of waves emitted by multiple point loads placed in the target region.

- In the TR step of experiment 1, we used Dirac delta functions to apply point loads at the sensor locations on the loaded boundary. In order to mimic the action of a number of finite-width sources applied on the ground surface, Karve et al. [19] used three pressure loads whose spatial description is given by Eq. (21). Hence, in the TR step of this experiment, we adopt Eq. (21) to describe the spatial variation of the horizontally polarized pressure loads. We compute the time signal for a pressure load by taking a weighted average of time-reversed signals recoded at the two sensors that are closest to the

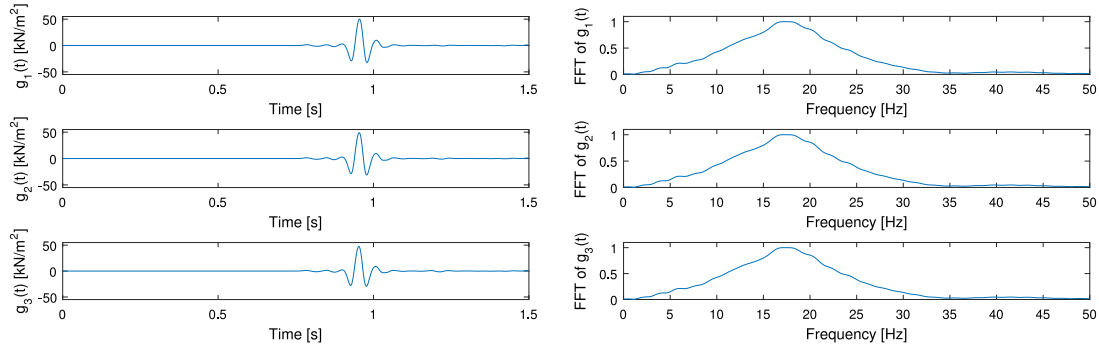

(a) Time signals for sources located at (−5, 0) m, (0, 0) m, and (7, 0) m, respectively.

(b) Frequency spectra for sources located at (−5, 0) m, (0, 0) m, and (7, 0) m, respectively.

Fig. 15. Source time signals and frequency spectra— TR1.

Table 4
Comparison between wave sources designed using the time-reversal approach and the inverse-source problem approach.

Approach/Method	Source time signals	Source locations [m]	KE_{inc}^{avg} [J/m]	E_{input} [J/m]	KE_{inc}^{avg}/E_{input}
IS1	Fig. 10	(−5, 0), (0, 0), (7, 0)	3.96	2561.76	1.55×10^{-3}
IS2	Fig. 10	(−20.04, 0), (−19.16, 0), (−19, 0)	4.98	3385.19	1.38×10^{-3}
IS3	Fig. 11	(−26.5, 0), (−25.2, 0), (−18.1, 0)	6.55	6587.05	9.94×10^{-4}
TR1	Fig. 15	(−5, 0), (0, 0), (7, 0)	0.55	93.96	5.89×10^{-3}
TR2	Fig. 16	(−20.04, 0), (−19.16, 0), (−19, 0)	0.69	152.82	4.51×10^{-3}
TR3	Fig. 17	(−26.5, 0), (−25.2, 0), (−18.1, 0)	0.69	116.88	5.94×10^{-3}

centerline of the load. That is, if x_i^c is the x_1-coordinate of the centerline of the i-th load, then

$$g_i(t) = A_o \left[\left(\frac{x_i^c - x_j}{x_{j+1} - x_j} \right) u_1(x_j, 0, T - t) + \left(\frac{x_{j+1} - x_i^c}{x_{j+1} - x_j} \right) u_1(x_{j+1}, 0, T - t) \right], \tag{35}$$

where x_js are the x_1-coordinates of the sensors ($-40 < x_j < x_i^c < x_{j+1} < 40$), and the constant A_o is chosen such that the maximum amplitude of the load is equal to 50 kN/m^2. In this manner, only a few sensors installed on the free (ground) surface form the time-reversal mirror.

Thus, in the forward step, we apply horizontally polarized point loads at all computational nodes within the target inclusion. Temporally, the loads vary like the modified Ricker pulse (Eq. (34), Fig. 8(a)). The time signals computed using Eq. (35) and the frequency spectra for each of the three loading cases (TR1, TR2, and TR3) are depicted in Figs. 15 through 17. We use surface loads characterized by these source signals to initiate the wave motion. The plots of the induced $KE_{inc}(t)$ and KE_{TA} are shown in Figs. 18 through 20. The values of the motion metrics for the TR and inverse-source algorithms are compared in Table 4. The CW-like time signals obtained using the inverse-source algorithm are able to deliver more kinetic energy (KE_{inc}^{avg}) in the time-averaged sense. Note that we used the same maximum amplitude of pressure loads for both the TR and the inverse-source algorithms. Furthermore, our definition of the time-averaged kinetic energy (KE_{inc}^{avg}) computes the average kinetic energy of the inclusion only for the duration for which it was excited. Thus, the motion metric has been normalized to eliminate the disadvantage of pulse-like excitations commonly used in the TR method.

It is clear that the wave sources suggested by the IS approach are able to deliver more kinetic energy to the inclusion. When the maximum source amplitudes are restricted due to equipment limitations and the application demands a strong shaking of the target formation, the IS method seems to be a more suitable algorithm for designing the wave sources. The higher yield achieved by the wave sources designed using the IS method does come at the cost of a higher input energy (E_{input}). When the efficiency of the energy delivery is considered, the pulse-like TR excitations outperform the CW-like excitations computed using the inverse-source approach. We remark that the inverse-source algorithm used in this comparison was formulated in order to maximize the velocity field in the target inclusion without any regard to the mechanical energy expended by the sources. A suitable motion metric that attempts maximization of the energy delivery while simultaneously minimizing the input energy can be used in the inverse-source approach to increase the efficiency of wave energy delivery.

3.4. Numerical experiment 3

In this experiment, we compare the intensity and efficiency of wave energy delivery achieved by wave sources whose temporal characteristics are described either by CW-like signals, or by pulse-like signals. We use three horizontally polarized

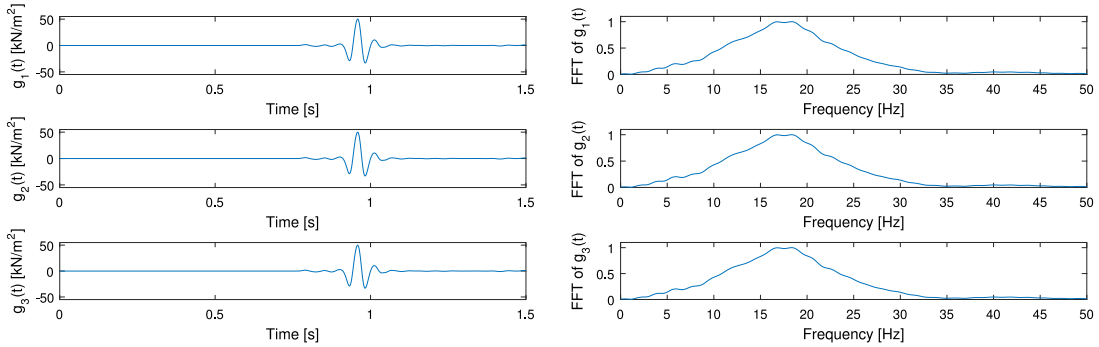

(a) Time signals for sources located at (−20.04, 0) m, (−19.16, 0) m, and (−19, 0) m, respectively.

(b) Frequency spectra for sources located at (−20.04, 0) m, (−19.16, 0) m, and (−19, 0) m, respectively.

Fig. 16. Source time signals and frequency spectra—TR2.

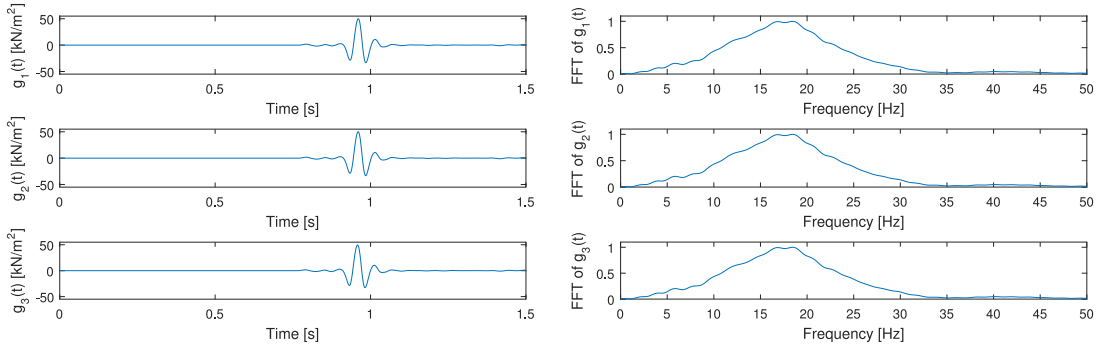

(a) Time signals for sources located at (−26.5, 0) m, (−25.2, 0) m, and (−18.1, 0) m, respectively.

(b) Frequency spectra for sources located at (−26.5, 0) m, (−25.2, 0) m, and (−18.1, 0) m, respectively.

Fig. 17. Source time signals and frequency spectra—TR3.

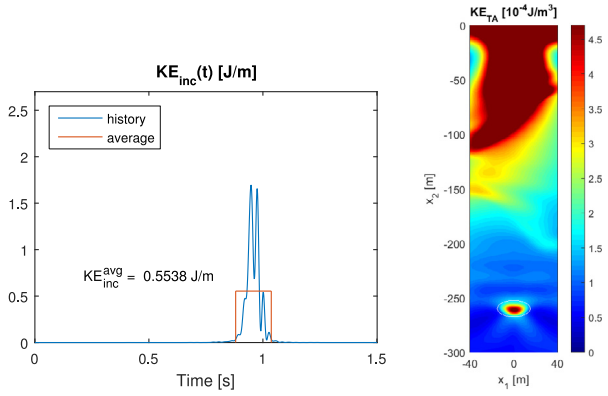

(a) History of KE_{inc}.

(b) KE_{TA}.

Fig. 18. $KE_{inc}(t)$ and KE_{TA} after using sources designed using the TR method (TR1).

surface loads centered at $(-5, 0)$, $(0, 0)$, and $(7, 0)$. Note that the choice of source locations is just a guess. We use Eq. (21) to describe the spatial variation of the horizontally polarized pressure loads, and the maximum amplitude is set at 50 kN/m^2. We consider the following temporal descriptions:

1. A modified Ricker pulse with $f_0 = 30$ Hz (Eq. (34), pulse-like),
2. The time signals used in the TR1 case (Fig. 15, pulse-like),
3. A monochromatic signal at the amplification frequency, i.e., at 18 Hz (CW-like), and
4. The time signals used in the IS1 case (Fig. 10, CW-like).

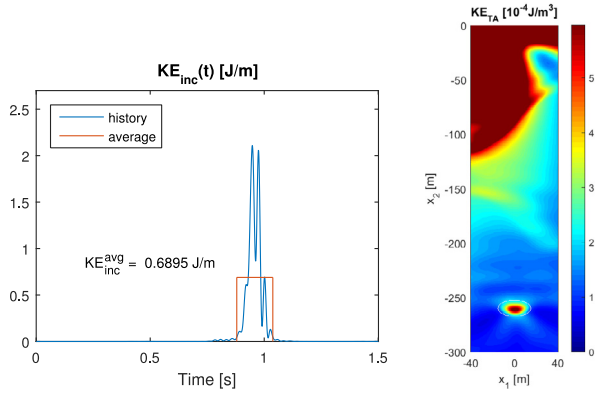

(a) History of KE_{inc}. (b) KE_{TA}.

Fig. 19. $KE_{inc}(t)$ and KE_{TA} after using sources designed using the TR method (TR2).

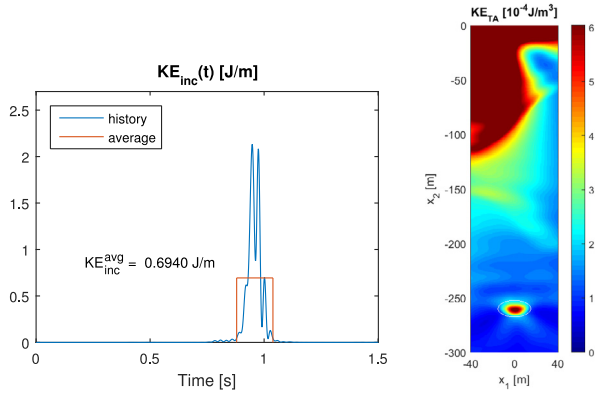

(a) History of KE_{inc}. (b) KE_{TA}.

Fig. 20. $KE_{inc}(t)$ and KE_{TA} after using sources designed using the TR method (TR3).

We use each of the above time signals as the driver signals for the three horizontally polarized surface sources, and compute the motion metrics for each case. The results are given in Table 5. It can be seen in Table 5 that as far as the value of KE_{inc}^{avg} is concerned, the CW-like signals outperform the pulse-like signals. The signals computed using the inverse-source approach (IS1), which aims at maximization of the velocity field in the target, deliver the highest amount of kinetic energy (in a time-averaged sense) to the target inclusion. The efficiency of wave energy delivery (KE_{inc}^{avg}/E_{input}) for sources driven by pulse-like signals is about four- to nine-times better than that for the CW-like signals. The modified Ricker pulse with the central frequency of 30 Hz, which was merely a guess, is the most efficient signal. Note that the pulse-like signal designed using the TR method delivers about 23% more kinetic energy to the target as compared to the guess. In geophysical applications of wave energy focusing, the stimulation is applied for days. Thus, a 23% increase in wave energy delivery is significant. This experiment highlights the interplay between two important aspects of wave energy delivery to subsurface formations: (a) the amount of energy delivered, and (b) the efficiency of wave energy delivery. Wave sources designed to achieve the highest efficiency may fail to breach the wave motion magnitude required to affect the desirable changes in the target formation. On the other hand, inefficiency in wave energy delivery may make the process economically infeasible. A judicious decision about the wave source design can be taken based on the requirements of the application in question. If a higher energy yield is desirable, and the efficiency of the process is of secondary importance, then CW-like source signals may be used. On the other hand, if a lower value of the time-averaged kinetic energy of the target is sufficient for the success of the underlying application, then pulse-like signals may deliver wave energy efficiently.

4. Conclusions

In this article, we studied the effectiveness of the time-reversal method in semi-infinite, elastic media using a numerical surrogate for the TR procedure. Despite the limited extent of the TR mirror, and the loss of wave energy directed away from the mirror, the TR method was able to achieve a good quality refocus. We observed that if the size of the time-reversal mirror stays the same, i.e., if the mirror covers the same length on the boundary, the ratio of KE_{inc}^{avg} to E_{input} does not change.

Table 5
Comparison between wave sources driven by pulse-like and CW-like time signals.

Approach/Method	Source time signals	Source locations [m]	KE_{inc}^{avg} [J/m]	E_{input} [J/m]	KE_{inc}^{avg}/E_{input}
Guess	Ricker pulse ($f_0 = 30$ Hz)	$(-5, 0), (0, 0), (7, 0)$	0.42	45.07	9.26×10^{-3}
TR1	Fig. 15	$(-5, 0), (0, 0), (7, 0)$	0.55	93.96	5.89×10^{-3}
Frequency sweep	Monochromatic ($f = 18$ Hz)	$(-5, 0), (0, 0), (7, 0)$	2.29	2006.09	1.10×10^{-3}
IS1	Fig. 10	$(-5, 0), (0, 0), (7, 0)$	3.96	2561.76	1.55×10^{-3}

That is, both KE_{inc}^{avg} and E_{input} are reduced by a factor proportional to the square of the number of sensors/sources used. We experimented with CW-like (narrow band) and pulse-like (wide band) signals in the forward step. The wide band forward step signal allowed the TR signal to be biased towards the amplification frequency. This resulted in a five-fold improvement in the efficiency of the energy delivery (KE_{inc}^{avg}/E_{input}). Finally, we compared the performance of wave sources designed using the TR and IS algorithms in the context of wave energy delivery to targeted subsurface formations. The IS approach is computationally demanding, and necessitates *a priori* knowledge of material and geometric properties of the domain of interest. It is capable of computing the optimal spatio-temporal characteristics of the wave sources, where optimality is defined based on minimization of a user-specified motion metric of the target zone. The flexibility in the choice of the motion metric is a critical advantage afforded by the IS method. Time-reversal (TR) is a self-adaptive method that can lead to the definition of wave source parameters so that the emitted wave energy is focused into the target zone. If placing wave sources in the target zone is a viable option, then the TR methodology, which does not rely on *a priori* knowledge of the material and geometric properties of the domain of interest, has an advantage. Our numerical experiments showed that the optimal source characteristics suggested by the IS algorithm achieve higher kinetic energy yield (in a time-averaged sense). The time signals suggested by the TR algorithm exhibit a higher KE_{inc}^{avg}/E_{input} ratio, and hence, higher efficiency. In applications of wave energy focusing to subsurface formations, a suitable algorithm for designing the wave sources can be chosen based on the expected energy yield, efficiency of wave energy delivery, and other practical considerations (e.g., viability of source placement in the target, the maximum allowable amplitude of the wave sources, etc.).

Acknowledgment

The authors' work was partially supported by an Academic Alliance Excellence grant between the King Abdullah University of Science and Technology in Saudi Arabia (KAUST) and the University of Texas at Austin. The support is gratefully acknowledged.

References

[1] A. Parvulescu, C.S. Clay, Reproducibility of signal transmission in the ocean, Radio Electron. Eng. 29 (1965) 223–228. http://dx.doi.org/10.1049/ree.1965.0047.
[2] M. Fink, Time reversal of ultrasonic fields—part I: Basic principles, IEEE Trans. Ultrason. Ferroelectr. Freq. Control 39 (5) (1992) 555–566. http://dx.doi.org/10.1109/58.156174.
[3] C. Draeger, M. Fink, One-channel time reversal of elastic waves in a chaotic 2D-silicon cavity, Phys. Rev. Lett. 79 (3) (1997) 407.
[4] C. Draeger, D. Cassereau, M. Fink, Theory of the time-reversal process in solids, J. Acoust. Soc. Am. 102 (3) (1997) 1289–1295.
[5] D. Givoli, E. Turkel, Time reversal with partial information for wave refocusing and scatterer identification, Comput. Methods Appl. Mech. Engrg. 213–216 (2012) 223–242. http://dx.doi.org/10.1016/j.cma.2011.12.005.
[6] D. Givoli, Time reversal as a computational tool in acoustics and elastodynamics, J. Comput. Acoust. 22 (03) (2014) 1430001. http://dx.doi.org/10.1142/S0218396X14300011.
[7] G.A. McMechan, Determination of source parameters by wavefield extrapolation, Geophys. J. Int. 71 (3) (1982) 613–628. http://dx.doi.org/10.1111/j.1365-246X.1982.tb02788.x.
[8] B.E. Anderson, M. Griffa, T.J. Ulrich, P.A. Johnson, Time reversal reconstruction of finite sized sources in elastic media, J. Acoust. Soc. Am. 130 (4) (2011) EL219–EL225.
[9] G. Derveaux, G. Papanicolaou, C. Tsogka, Time reversal imaging for sensor networks with optimal compensation in time, J. Acoust. Soc. Am. 121 (4) (2007) 2071–2085. http://dx.doi.org/10.1121/1.2536888.
[10] E. Amitt, D. Givoli, E. Turkel, Time reversal for crack identification, Comput. Mech. 54 (2) (2014) 443–459.
[11] P.D. Norville, W.R. Scott Jr., Time-reversal focusing of elastic surface waves, J. Acoust. Soc. Am. 118 (2) (2005) 735–744.
[12] B.E. Anderson, R.A. Guyer, T.J. Ulrich, P.A. Johnson, Time reversal of continuous-wave, steady-state signals in elastic media, Appl. Phys. Lett. 94 (11) (2009) 111908.
[13] D. Cassereau, M. Fink, Focusing with plane time-reversal mirrors: An efficient alternative to closed cavities, J. Acoust. Soc. Am. 94 (4) (1993) 2373–2386. http://dx.doi.org/10.1121/1.407457.
[14] F. Wu, J.-L. Thomas, M. Fink, Time reversal of ultrasonic fields—part II: Experimental results, IEEE Trans. Ultrason. Ferroelectr. Freq. Control 39 (5) (1992) 567–578. http://dx.doi.org/10.1109/58.156175.
[15] B.E. Anderson, M. Griffa, C. Larmat, T.J. Ulrich, P.A. Johnson, Time reversal, Acoust. Today 4 (1) (2008) 5–16.
[16] M. Fink, et al., Time-reversed acoustics, Sci. Am. 281 (5) (1999) 91–97.
[17] A.M. Sutin, J.A. TenCate, P.A. Johnson, Single-channel time reversal in elastic solids, J. Acoust. Soc. Am. 116 (5) (2004) 2779–2784.
[18] C. Jeong, L. Kallivokas, S. Kucukcoban, W. Deng, A. Fathi, Maximization of wave motion within a hydrocarbon reservoir for wave-based enhanced oil recovery, J. Pet. Sci. Eng. 129 (0) (2015) 205–220. http://dx.doi.org/10.1016/j.petrol.2015.03.009.
[19] P.M. Karve, S. Kucukcoban, L.F. Kallivokas, On an inverse source problem for enhanced oil recovery by wave motion maximization in reservoirs, Comput. Geosci. 19 (1) (2015) 233–256. http://dx.doi.org/10.1007/s10596-014-9462-7.
[20] P.M. Karve, L.F. Kallivokas, Wave energy focusing to subsurface poroelastic formations to promote oil mobilization, Geophys. J. Int. 202 (1) (2015) 119–141. http://dx.doi.org/10.1093/gji/ggv133.

[21] P.M. Karve, A. Fathi, B. Poursartip, L.F. Kallivokas, Source parameter inversion for wave energy focusing to a target inclusion embedded in a three-dimensional heterogeneous halfspace, in: International Journal for Numerical and Analytical Methods in Geomechanics (submitted for publication).
[22] P.M. Karve, L.F. Kallivokas, L. Manuel, A framework for assessing the uncertainty in wave energy delivery to targeted subsurface formations, J. Appl. Geophys. 125 (2016) 26–36.
[23] I. Levi, E. Turkel, D. Givoli, Time reversal for elastic wave refocusing and scatterer location recovery, J. Comput. Acoust. 23 (01) (2015) 1450013. http://dx.doi.org/10.1142/S0218396X14500131.
[24] S. Kucukcoban, L. Kallivokas, A symmetric hybrid formulation for transient wave simulations in PML-truncated heterogeneous media, Wave Motion 50 (1) (2013) 57–79.
[25] S.A. Kostrov, B.O. Wooden, Mechanisms, field suitability, and case studies for enhancement of oil recovery and production using in-situ seismic stimulation, in: 16th International Symposium on Nonlinear Acoustics, 2002.
[26] P.M. Roberts, E.L. Majer, W.-C. Lo, G. Sposito, T.M. Daley, An integrated approach to seismic stimulation of oil reservoirs: Laboratory, field and theoretical results from doe/industry collaborations, in: 16th International Symposium on Nonlinear Acoustics, 2002.
[27] P.M. Roberts, A.I. Abdel-Fattah, Seismic stress stimulation mobilizes colloids trapped in a porous rock, Earth Planet. Sci. Lett. 284 (3) (2009) 538–543.
[28] I. Beresnev, W. Gaul, R.D. Vigil, Direct pore-level observation of permeability increase in two-phase flow by shaking, Geophys. Res. Lett., 38 (20) http://dx.doi.org/10.1029/2011GL048840.
[29] T. Candela, E.E. Brodsky, C. Marone, D. Elsworth, Laboratory evidence for particle mobilization as a mechanism for permeability enhancement via dynamic stressing, Earth Planet. Sci. Lett. 392 (0) (2014) 279–291. http://dx.doi.org/10.1016/j.epsl.2014.02.025.
[30] S. Yon, M. Tanter, M. Fink, Sound focusing in rooms: The time-reversal approach, J. Acoust. Soc. Am. 113 (3) (2003) 1533–1543. http://dx.doi.org/10.1121/1.1543587.
[31] J.D. Maynard, E.G. Williams, Y. Lee, Nearfield acoustic holography: I. theory of generalized holography and the development of NAH, J. Acoust. Soc. Am. 78 (4) (1985) 1395–1413. http://dx.doi.org/10.1121/1.392911.